Pore anisotropy in shale and its dependence on thermal maturity and organic carbon content

A scanning SAXS study

Bahadur, Jitendra; Chandra, Debanjan; Das, Avik; Vishal, Vikram; Agrawal, Ashish Kumar; Sen, Debasis

DOI
10.1016/j.coal.2023.104268

Publication date
2023

Document Version
Final published version

Published in
International Journal of Coal Geology

International Journal of Coal Geology 273 (2023) 104268

Contents lists available at ScienceDirect

International Journal of Coal Geology

journal homepage: www.elsevier.com/locate/coal

Pore anisotropy in shale and its dependence on thermal maturity and organic carbon content: A scanning SAXS study

Jitendra Bahadur [a,b,*], Debanjan Chandra [c], Avik Das [a], Vikram Vishal [d,e,f,**], Ashish Kumar Agrawal [g], Debasis Sen [a,b]

[a] Solid State Physics Division, Bhabha Atomic Research Centre, Mumbai 400085, India
[b] Homi Bhabha National Institute, Anushaktinagar, Mumbai 400094, India
[c] Department of Geoscience and Engineering, Delft University of Technology, Delft 2628 CN, the Netherlands
[d] Computational and Experimental Geomechanics Laboratory, Department of Earth Sciences, Indian Institute of Technology Bombay, Mumbai 400076, India
[e] National Centre of Excellence in Carbon Capture and Utilization, Indian Institute of Technology Bombay, Mumbai 400076, India
[f] Interdisciplinary Programme in Climate Studies, Indian Institute of Technology Bombay, Mumbai 400076, India
[g] Technical Physics Division, Bhabha Atomic Research Centre, Mumbai 400085, India

ARTICLE INFO

Keywords:
Shale
Small-angle X-ray scattering
Anisotropy
Heterogeneity
FTIR
X-ray CT

ABSTRACT

Pore orientation in shale governs the fluid transport properties that are key to hydrocarbon production and potential CO_2 sequestration. The present work deals with the detailed study of nano-heterogeneities in shales, across the bedding plane, of varying thermal maturity and total organic carbon content using scanning small-angle X-ray scattering (SAXS) experiments. The complementary X-ray Micro-Computed Tomography (μCT) and functional group mapping elucidate the heterogeneity in micrometer resolution. 2D SAXS profiles of the shales show elliptical patterns indicating the nanoscale pore anisotropy in shale. The orientation of pores and their spatial variation is strongly dependent on the content of organic matter. The variance in the anisotropy parameter is validated with chemical mapping and high-resolution 3D imaging.

1. Introduction

Shales are emerging unconventional reservoirs for hydrocarbons and have also potential to seal carbon dioxide (Busch et al., 2008; Chareonsuppanimit et al., 2012; Kang et al., 2011), and nuclear waste in the subsurface for permanent sequestration (Liu, 2014; Neuzil, 2013). The prediction of storage capacity and suitability of shale for CO_2 and nuclear waste disposal is associated with the porosity and pore size distributions in shale. The role of pore anisotropy, due to preferred orientations of mineral and organic matter, on the hydrocarbon generation and CO_2 sequestration capacity is well understood (Cao et al., 2019; Kwon et al., 2004; Yin et al., 2020; Zhang et al., 2021; Zhang et al., 2020). Knowledge of the orientation of the nano-heterogeneity in shale is crucial for predicting transport properties, and gas storage potential (Bhandari et al., 2015; Cui and Si, 2021; He et al., 2022; Zhang et al., 2017). Naturally occurring sedimentary rocks are heterogeneous and shale reservoirs are no different. The intrinsic vertical (bedding perpendicular) anisotropy arises due to the depositional environment, and preferential orientation of clay minerals and organic matter. Post-deposition rearrangement of clastic fragments, clay minerals, and formation of fine layering due to overburden pressure is termed induced anisotropy (Sayers, 2013). The preferred orientation of pores in shales is a consequence of mechanical stress primarily by the weight of the overlying sediments. A complex pore structure in the shale with dimensions ranging from micrometer to nanometer scale (Bahadur et al., 2016; Bahadur et al., 2014; Bahadur et al., 2015). The pores in the shales are classified as macropores (> 50 nm), mesopores (2–50 nm), and micropores (< 2 nm) (Rouquerol et al., 1994). The micropores are most abundant in shales that contain adsorbed gas and this contributes to the largest fraction of storage capacity (Chalmers and Bustin, 2007; Chalmers et al., 2012; Gasparik et al., 2014; Gasparik et al., 2012; Vishal et al., 2019). Compaction reduces porosity with depth depending on the compressibility of the sediment. The compaction of shale flattens the pores parallel to the bedding plane (Blach et al., 2020; Hall and Mildner,

* Correspondence to: Jitendra Bahadur, Solid State Physics Division, Bhabha Atomic Research Centre, Mumbai 400085, India.
** Correspondence to: Vikram Vishal, Computational and Experimental Geomechanics Laboratory, Department of Earth Sciences, Indian Institute of Technology Bombay, Mumbai 400076, India.
E-mail addresses: jbahadur@barc.gov.in (J. Bahadur), v.vishal@iitb.ac.in (V. Vishal).

https://doi.org/10.1016/j.coal.2023.104268
Received 31 January 2023; Received in revised form 17 May 2023; Accepted 17 May 2023
Available online 19 May 2023

1983; Reynolds and Mildner, 1984). The anisotropy is closely linked to the chemical and physical heterogeneity of the shale (Blach et al., 2020; Kwon et al., 2004). The gas adsorption capacity of the shale depends on the pore volume, pore surface area, and porosity. However, the accessibility and permeability of pore networks are other important parameters (Ma et al., 2016; Zhang et al., 2020). The preferred orientation of mineral and organic matter in the bedding plane can create pathways for fluid flow and affects the accessibility of the adsorption sites (Ma et al., 2016). This preferred orientation results in a non-uniform distribution of pore spaces, with some more open, interconnected pores, while others are more densely packed and less permeable in directional variations in the gas adsorption capacity of shale, with some directions exhibiting higher or lower adsorption than others (Kwon et al., 2004; Ma et al., 2016; Zhang et al., 2021).

Small-angle neutron scattering (SANS) is a widely used technique to probe the pore structure in the shale (Radlinski et al., 2004; Radlinski, 2006). Using contrast matching SANS, the accessibility of pores in the length scale ranging from μm to nm in shales has been previously investigated (Bahadur et al., 2018; He et al., 2012; Mastalerz et al., 2012; Ruppert et al., 2013). Small-angle X-ray scattering (SAXS) alone cannot distinguish between accessible and inaccessible pores but combined with gas adsorption techniques, it can do so (Chandra et al., 2023; Chandra et al., 2022; Chandra et al., 2020a). The structural anisotropy in shales was studied using SANS and SAXS (Anovitz et al., 2015; Gu et al., 2015). The large X-ray flux at synchrotron sources allows beam sizes in the order of μm and resolves the spatial distribution of anisotropy with μm resolution (Leu et al., 2016). In the last few decades, X-ray CT imaging has emerged as a powerful tool to resolve micrometer-scale features in different rock types, however, visualizing nm-scale pores in shales is difficult with such methods. X-ray CT has been extensively used to characterize 3D microstructures and fractures in shales, which contributed to improving the understanding of shale as a reservoir (Al Shafloot et al., 2021; Arif et al., 2021; Chandra and Vishal, 2021; Duan et al., 2022; Vishal and Chandra, 2022).

In this work, scanning SAXS measurements have been carried out on a slice of shale cut perpendicular to the bedding plane. Standard SAXS measurements involve powdered shale samples to understand the pore structure (which produces an isotropic SAXS pattern, which is easier to process); however, limited studies have been performed with intact shale specimens. The analysis of the 2D anisotropic SAXS pattern produced by intact shale specimens is challenging and therefore limited information for shale pore structure could be extracted so far. In this work, pore orientation is analyzed by a conventional approach using azimuthally averaged SAXS profiles as well as by an advanced approach involving isosize analysis of the sectorial radially averaged SAXS profiles developed recently (Blach et al., 2020). The scanning SAXS experiments provide evidence of the varying the pore orientation and its direction concerning the direction of the incident X-ray beam. The chosen shale samples vary in thermal maturity, mineral composition, and total organic content. FTIR chemical mapping and X-ray microtomography have been carried out to study chemical and physical heterogeneity linked with pore heterogeneity (Fig. 1).

2. Samples and methodology

The five studied (BK5, BK12, B37, BK38, and BKU) shale samples belong to the Cisuralian Barakar Formation collected from an active drilling site in Asansol, West Bengal, India. The geology of the sampling location along with the depths of occurrence of the collected shales were discussed in earlier studies (Chandra et al., 2022). Depth-dependent bulk geochemistry, pore attributes, and composition of shales from similar areas have also been reported in previous studies (Chandra and Vishal, 2020; Chandra et al., 2020b), which indicates clear dominance of clay minerals and organic matter on mesopore and micropore attributes respectively. The Barakar shales were formed under the complex fluvial depositional environment studied in repetitive fining upwards depositional cycles that were affected by lateral channel migration (Bhattacharjee et al., 2018; Bhattacharya et al., 2012; Sen and Dey, 2019). The organo-petrographic character and the depth-dependent maceral composition of Barakar shales reveal that the organic-rich, clay-dominated shales were formed under a passive continental margin setting and have fairly good potential for oil generation (Varma et al., 2018). Chemical and pore heterogeneity of these shales parallel to bedding planes have been reported in (Chandra et al., 2022), where the authors

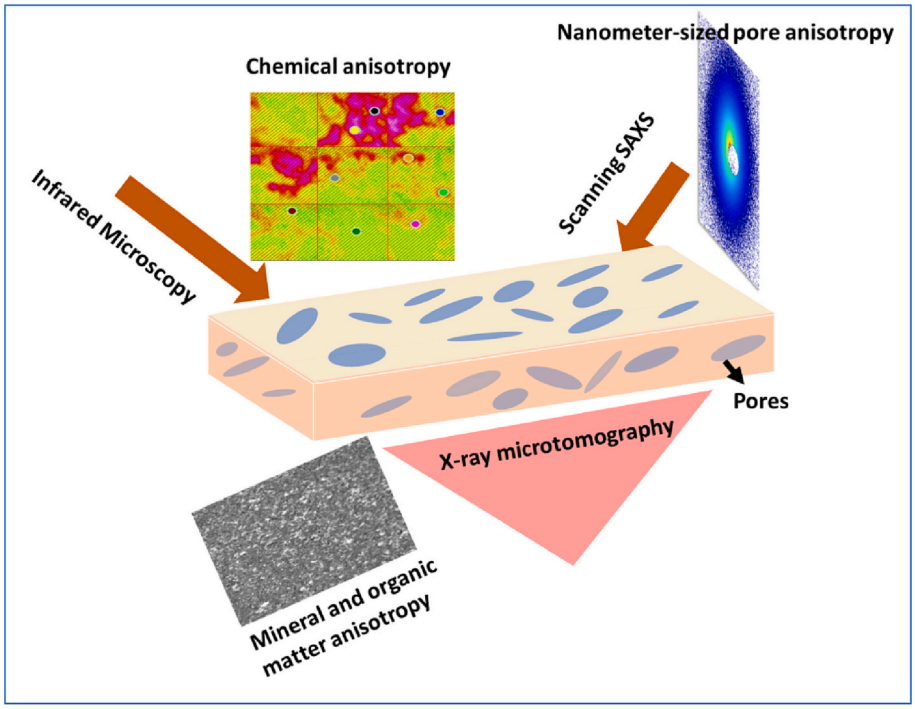

Fig. 1. Techniques utilized in the study. Pores are aligned along the bedding of the shale.

concluded that the degree of heterogeneity in bedding parallel direction increases with increasing thermal maturity of the shales. These shale slices were prepared by cutting the bedding plane and subsequently trimmed and polished to maintain a uniform size of 10 × 10 × 1 mm^3., and The samples 'thermal maturity and total organic content (TOC) were estimated using Rock-Eval 6 (Table 1). In Rock-Eval experiments, the thermal maturity is signified as the temperature where the highest amounts of volatiles are produced during anoxic heating (Lafargue et al., 1998). Although the Tmax of BK12 is lower than the other shales, Chandra et al. (2022) demonstrated that both BK5 and BK12 have weak S2 curves, which are fingerprints for thermally induced alteration. A weak S2 curve makes Tmax calculations unreliable. Therefore, we used the oxidation stage S4Tpeak (Table 1) as a proxy for thermal maturity (Hazra et al., 2021), which indicates that BK5 and BK12 have higher maturity than the other shales.

2.1. Distribution of functional groups

Micro-attenuated total reflection (ATR) based Fourier transform infrared spectroscopy (FTIR), coupled with focal plane array (FPA) imaging, is used for visualizing the distribution of functional groups (Lewis et al., 1995). Pores in the organic matter of shales contribute most to the total pore volume (Chalmers and Bustin, 2007; Ji et al., 2017; Nie et al., 2018). The spatial distribution of organic functional groups qualitatively indicates the distribution of organic matter, thereby indicating pore localization. As opposed to bulk organic matter characterization, the ATR-FTIR method provides in-situ distribution of functional groups. Spectral data for each sample were collected within 700–4000 cm^{-1} wavenumber in a mapping area of 250 × 250 μm^2. Individual points spot measurements of 4 μm diameter were collected over the mapping region and further integrated to produce a false-color FPA map facilitated by an aperture-free liquid N_2-cooled mercury cadmium telluride (MCT) detector. Micro-ATR measurements were facilitated by a 20× Ge ATR lens of 1-in. diameter coupled with a Bruker 3000 Hyperion microscope. Chemical mapping and data processing were performed with Bruker OPUS software. Multiple spectra were acquired on the visible surface to highlight the functional group distribution throughout the imaging area. As discussed by Chandra et al. (2022), alkenes and aromatic C—H bonds are abundant in the organic matter, therefore the integration range for the FPA colormaps was chosen to be 900–1200 cm^{-1}.

2.2. High-resolution X-ray imaging

Spatial anisotropy of organic and mineral phases was investigated using a high-resolution synchrotron X-Ray micro-tomography (X-ray CT) at BL-4 (Imaging Beamline) of Indus-2 Synchrotron source, Raja Ramanna Centre for Advanced Technology (RRCAT), Indore (Agrawal et al., 2015) followed by 3D image analysis. A high-intensity parallel X-ray beam from a bending magnet synchrotron source (1.5 T) with a fiber-optic coupled high-resolution CCD camera of dimension 4000 × 2670 (voxel size 4.5 μm) was used. A beam energy of 20 keV and sample-to-detector distance of 250 mm was optimized for sufficient transmission through the sample with phase-contrast-based edge enhancement to attain the best differentiation between organic and mineral phases. A set of 900 projections were taken for each sample, rotating a full 180° at a rotation step of 0.2°. Individual projections were imported in Avizo for post-processing and image-based quantification. A uniform sub-volume from each reconstructed volume was extracted for mineral and organic matter quantification. A median filter and unsharp masking were applied sequentially on the reconstructed volume for removing noise and enhancing the contrast. As minerals have a higher density than organic matter, the attenuation coefficient is higher for mineral phases, resulting in brighter voxels. In contrast, due to its lower density, organic matter appears as darker voxels. These two phases were segmented using a grayscale threshold for relative volume quantification. Each 3D subvolume was further divided into 9 equal volumes for maintaining consistent grid-based quantification.

2.3. Small-angle X-ray scattering

Small-angle X-ray scattering (SAXS) study was carried out using a SWAXS beamline (Bahadur et al., 2019), BL-18, at the Indus-2 synchrotron, India. The X-ray energy was chosen as 16 KeV. Samples were mounted with a bedding plane direction parallel to the X-ray beam (horizontal) as shown in Fig. 2. The shale samples were partitioned into a 3 × 3 matrix, with each section measuring 3 mm × 3 mm. Scanning SAXS measurements were conducted using a 500 μm. X-ray beam on each section of the matrix. The experimental 2D SAXS data exhibited anisotropic characteristics, which are attributed to the preferential alignment of the pores.

2.4. Spatial resolution and scale of various mapping techniques

The crucial parameters in any technique, probing the heterogeneity in shale, are the minimum accessible length scale and spatial resolution. The typical size of the specimen required for the study is in the range of a few centimeters. The minimum resolution of optical microscopy is in the range of micrometers whereas the resolution of electron microscopy is in the range of a few nanometers. The minimum length scale accessible by SAXS/SANS is in the range of a few nanometers. The spatial resolution of SAXS/SANS is limited by the beam size of X-rays/neutrons. Electron microscopy is a surface-sensitive technique and therefore not suitable for the study of the heterogeneity of the bulk shale samples (Kwiecińska et al., 2019; Wang et al., 2014). Probing the spatial heterogeneity and anisotropy in shale using SANS is not possible due to the large beam size. SAXS overcomes this limitation to probe the spatial heterogeneity and pore alignment due to the availability of small X-ray beam sizes at synchrotron sources.

3. Results

3.1. In-situ functional group mapping

FPA imaging of the functional groups in bedding-perpendicular shale sections monitors the distribution of organic matter on bedding perpendicular shale section (Fig. 3a-e).

The distribution of organic functional groups in chemical maps is scattered unevenly in shales BK5 and BK12 (Fig. 3a,b). A preferred orientation of the functional groups on the 2D surface is evident from the images. The functional group distribution of all shales shows preferential horizontal elongation along the bedding plane (Fig. 3a-e).

The FTIR point spectra of BK5 shows high absorbance at ~1000

Table 1
Mineralogical composition, thermal maturity (Tmax), S4Tpeak, and TOC of the studied shale samples (Chandra et al., 2022).

Sample	Quartz (%)	Illite (%)	Kaolinite (%)	Orthoclase (%)	Siderite (%)	Tmax (°C)	S4Tpeak (°C)	TOC (%)
BK5	11	34	15	40	0	499	685	38.2
BK12	8	38	18	36	0	308	670	33.6
BK37	19	47	6	15	13	443	565	2.6
BK38	31	52	9	5	4	439	555	5.4
BKU	21	56	3	10	10	444	553	4.3

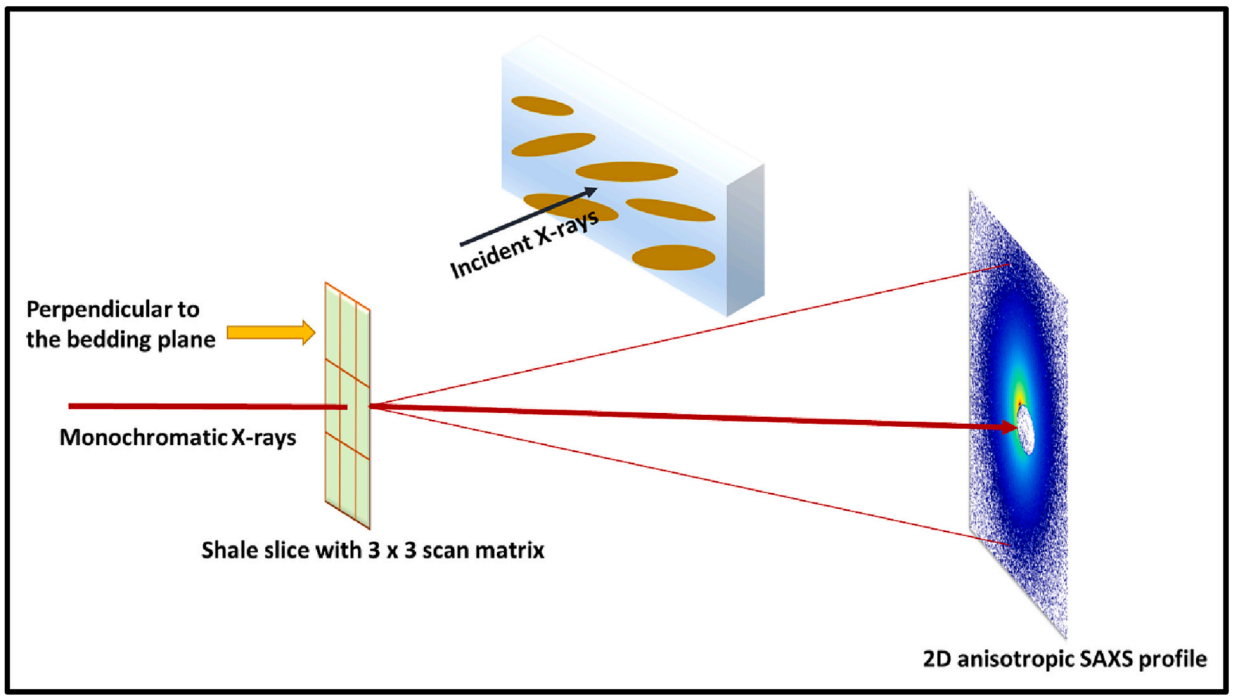

Fig. 2. Schematic of the SAXS set-up. The sample was mounted on an XY translation stage for scanning.

cm^{-1} wavenumber (Fig. 4a) which we (Chandra et al., 2022) explained as an indication of a higher thermal maturity. Contrary to BK5, BK12 shows peaks at ~1500 cm^{-1} and 1850 cm^{-1} indicating the presence of alkoxy, acyl, and phenyl C—O bonds (Fig. 4b) (Chen et al., 2016; Fan et al., 2015; Yan et al., 2013). The peak around 1850 cm^{-1} specifically indicates the presence of carboxyl and carbonyl groups (Chen et al., 2016). Compared to BK5 and BK12, BK37 and BK38 show a higher abundance of C—O bonds indicated by strong absorbance at ~1450 cm^{-1} wavenumber (Chen et al., 2016) (Fig. 4c, d). All shale samples showed a low signal-to-noise ratio in the 3000–4000 cm^{-1} range, possibly due to water loss or the presence of structural -OH groups in clay minerals (Fan et al., 2015; Yan et al., 2013).

3.2. X-ray Computed Tomography

Preferential alignment of the minerals and organic matter is observed along the bedding planes (Fig. 5a, b, c). The organic matter variability is quantified by the relative abundance of organic matter across different grid blocks (Fig. 5f).

3.3. Scanning SAXS analysis

The X-ray transmission values during the scanning SAXS measurements in a 3 × 3 matrix of shale are tabulated in Table S1 of the supporting information. The contour map of the transmission along with the X-ray radiograph of the shale samples is shown in the Fig. S1 of the supporting information. The spatial heterogeneity in the X-ray images is corroborated by the heterogeneity reflected in the transmission contour map. The transmission values in BK5 shale vary in the range of 0.3 to 0.5 with a maximum variation of 38% whereas the BK12 shows the highest level of heterogeneity where transmission varies in the range of 0.99 to 0.41. BK37 shows uniform transmission values across all the scan points. BK38 shows very poor transmission of X-ray and it varies in the range of 0.04 to 0.06 whereas BKU shows a moderate value of the transmission in the range of 0.15 to 0.34.

4. Discussion

4.1. Pore orientation from scanning SAXS

4.1.1. Azimuthal orientation of pores

The nanometer-sized heterogeneity across the bedding plane is reflected in the 2D SAXS pattern (Fig. 6a). an anisotropic pore structure results in elliptical isointensity profiles (Summerfield and Mildner, 1983). The degree of alignment of pores is estimated using the 2D SAXS profile. The azimuthal intensity plot as depicted in Fig. 6b shows the predominant orientation of the long axis of the pores. The scattering intensity as a function of wave vector transfer Q [defined as $4\pi\sin\theta/\lambda$ where 2θ is the scattering angle and λ is the wavelength of X-ray] along the major and minor axis is obtained by sectorial radial averaging. In the present work, the azimuthal averaging was performed in the Q-range of 0.4 and 1.3 nm^{-1} (Fig. 6a).

Two-phase approximation assumed that the electron density of the shale matrix is uniform. To check the validity, the scattering length density (SLD) of the mineral components of the shale is calculated for X-rays with 16 KeV. The calculated scattering length density (SLD) of the mineral components is shown in the Table S2 of the supporting information. It is seen that the SLD of the mineral constituents ranges from 2.1×10^{11} cm^{-2} to 2.3×10^{11} cm^{-2} except for siderite which has a higher SLD value of 3.2×10^{11} cm^{-2}. However, siderite is not present in BK5 and BK12 therefore mineral matrix of these two samples is considered uniform as far as its electron density is concerned. BK37, BK38, and BKU show the presence of siderite and therefore the two-phase approximation is a crude approximation for these three samples. If it is assumed that the length scale of the siderite component does not fall within the size range probed by SAXS, the variation in the SLD of siderite is unlikely to affect the extracted information related to the pore size distribution and its orientation. It is evident from tomography images that the typical size of the individual minerals is larger than a micrometer (Zhao et al., 2022) (Fig. 5). Therefore, scattering caused by the micron-sized siderite is not observed.

One of the simplest approaches to estimating the orientation of pores is an analysis of the peak areas of the azimuthal SAXS profiles. This approach has been extensively used to describe the orientation of the

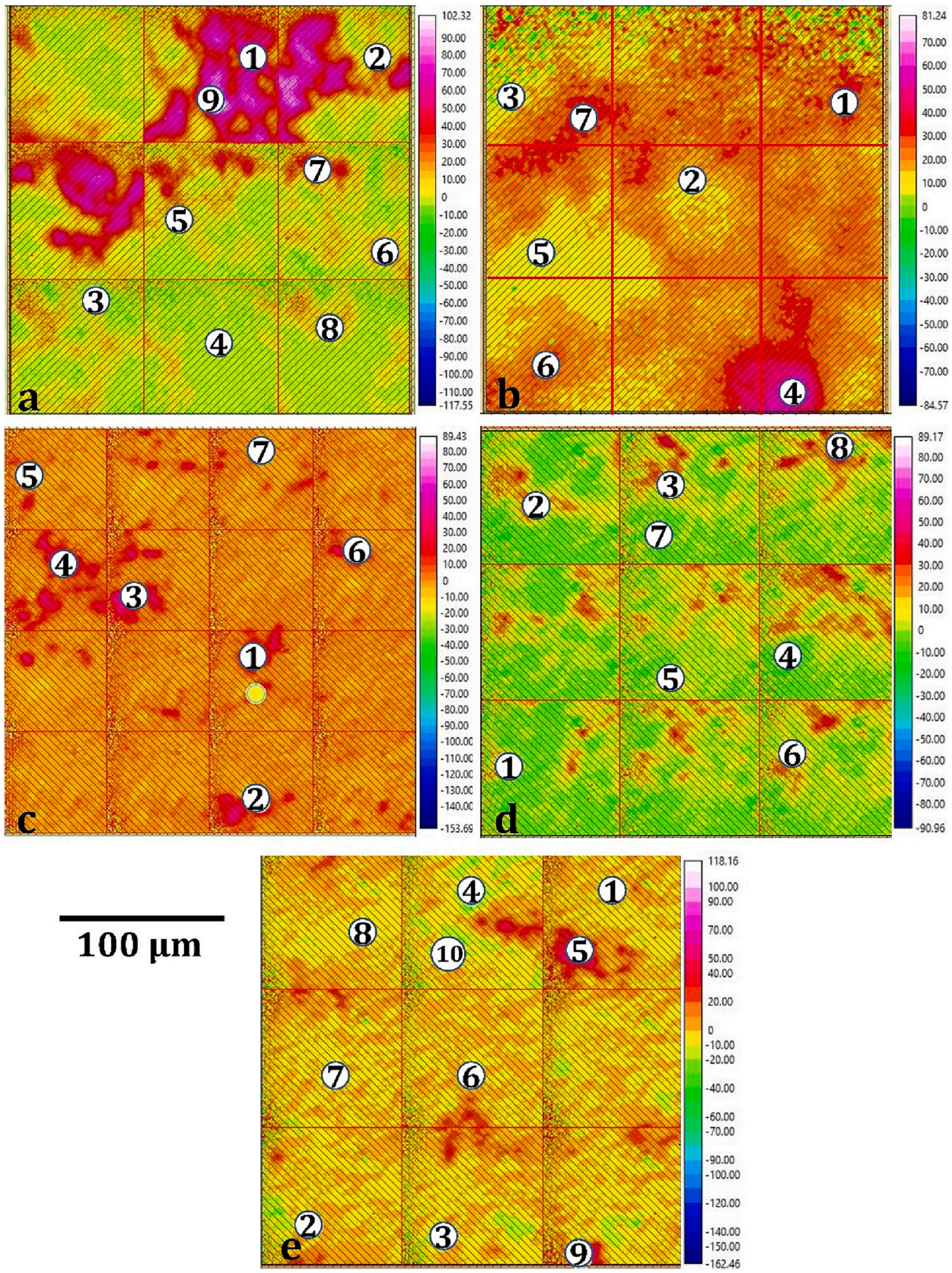

Fig. 3. Micro-ATR-based FPA chemical map of bedding perpendicular slices of shales. a-e represent FPA maps for BK5, BK12, BK37, BK38 and BKU respectively. The color bars indicate the intensity of each pixel in an integration range of 900–1200 cm^{-1}. Red colors represent the higher intensity of alkene and alkanes (signifying more organic matter) and vice versa. The IR spectra for each numbered point are shown in Fig. 4. (For interpretation of the references to color in this figure legend, the reader is referred to the web version of this article.)

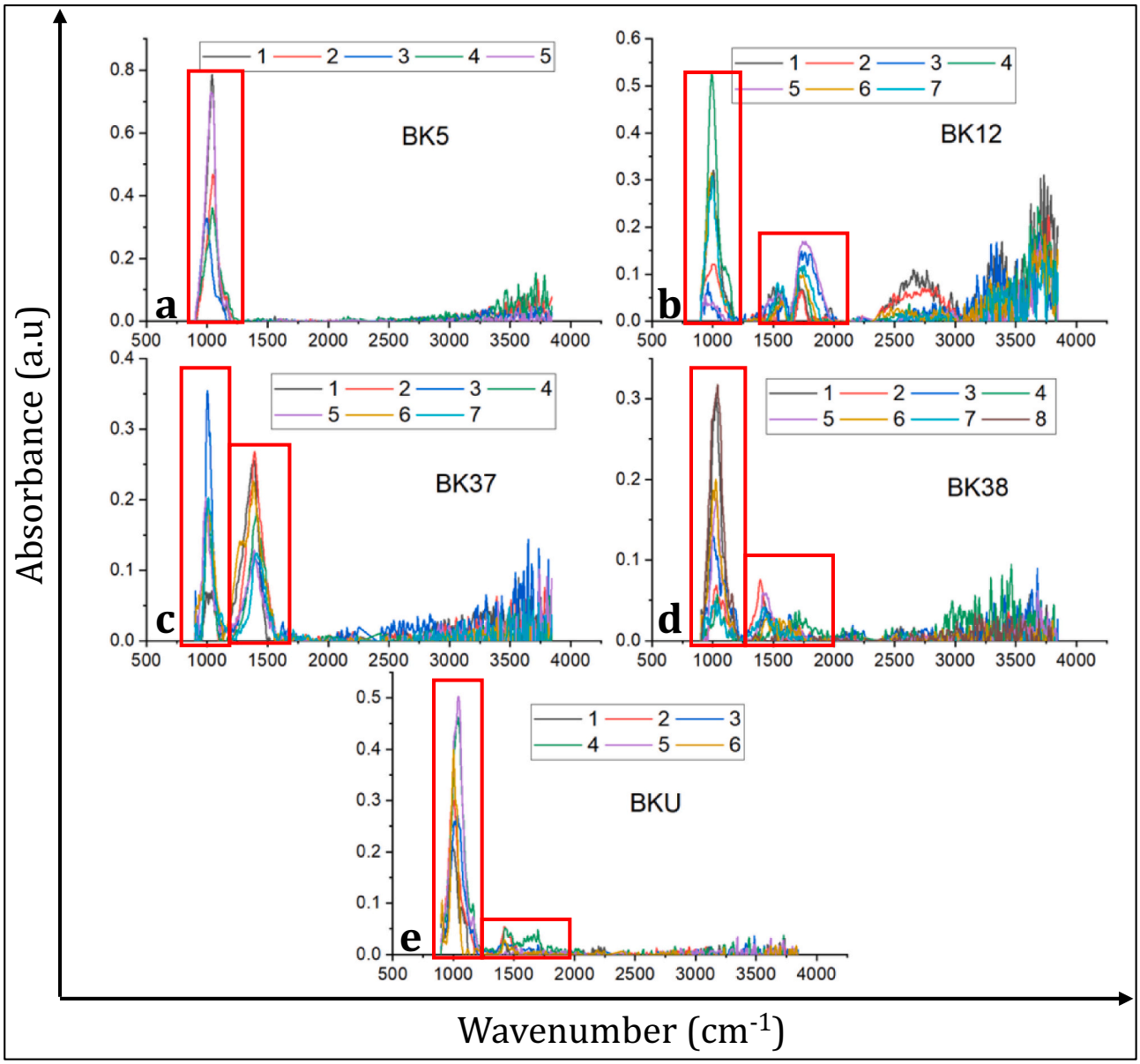

Fig. 4. FTIR spectra of individual points marked in Fig. 3 showing the presence of organic functional groups. Red boxes indicate the absorbance of alkene and alkanes, signifying the presence of organic matter. (For interpretation of the references to color in this figure legend, the reader is referred to the web version of this article.)

mineral nanoparticles in the collagen structure of the bone (Fratzl et al., 1992; Rinnerthaler et al., 1999; Turunen et al., 2014). The degree of orientation of pores ρ is defined as;

$$\rho = \frac{\Psi_1 + \Psi_2}{\Psi_1 + \Psi_2 + \Psi_0} \quad (1)$$

$\Psi_1 + \Psi_2$ is the sum of the area of two peaks separated by 180° whereas Ψ_0 is the area under the linear background, as marked in Fig. 5b. The area of the peaks was estimated by fitting the peak profile with a Gaussian function. This simplistic definition of the degree of pore orientation (Eq. (1)) does not assume any functional form of the scattering intensity I(Q) unlike the other established approaches used to describe the anisotropy in the shale (Blach et al., 2020; Gu and Mildner, 2016). The small variation in the SLD of the mineral components and scattering from organic matter-embedded micropores somewhat contributes to the high-Q flat scattering and it can slightly underestimate the degree of orientation. The degree of the pore alignment has been calculated for each scan of the 3 × 3 matrix in each shale sample and values are shown in Table S1 of the supporting information.

The azimuthal plots of the scattering intensity (Fig. 7a,d) of the organic-rich shale samples indicate the variation in the degree of pore orientation at different scan points. A contour plot of the degree of pore orientation (Fig. 7b, e) shows strong variation at different scan points. The azimuthal plot and contour map of the degree of orientation for shale with less TOC (Fig. 8a, d, g and Fig. 8b, e, h, respectively) show less variation in the degree of orientation at different scan points. It is expected that the pressing of pores over geological time is caused by compaction that gives rise to a unique axis perpendicular to the bedding plane. However, the orientations of the pores in the bedding plane also depend on the matrix. Compaction and sedimentation processes, both affect the pore orientation. Therefore, the unique axis of the anisotropy may not be uniform spatially on the nanometer scale. The scanning SAXS resolves the spatial distribution in the unique axis pore orientation. The 2D SAXS profiles obtained from the 3 × 3 shale matrix show variations

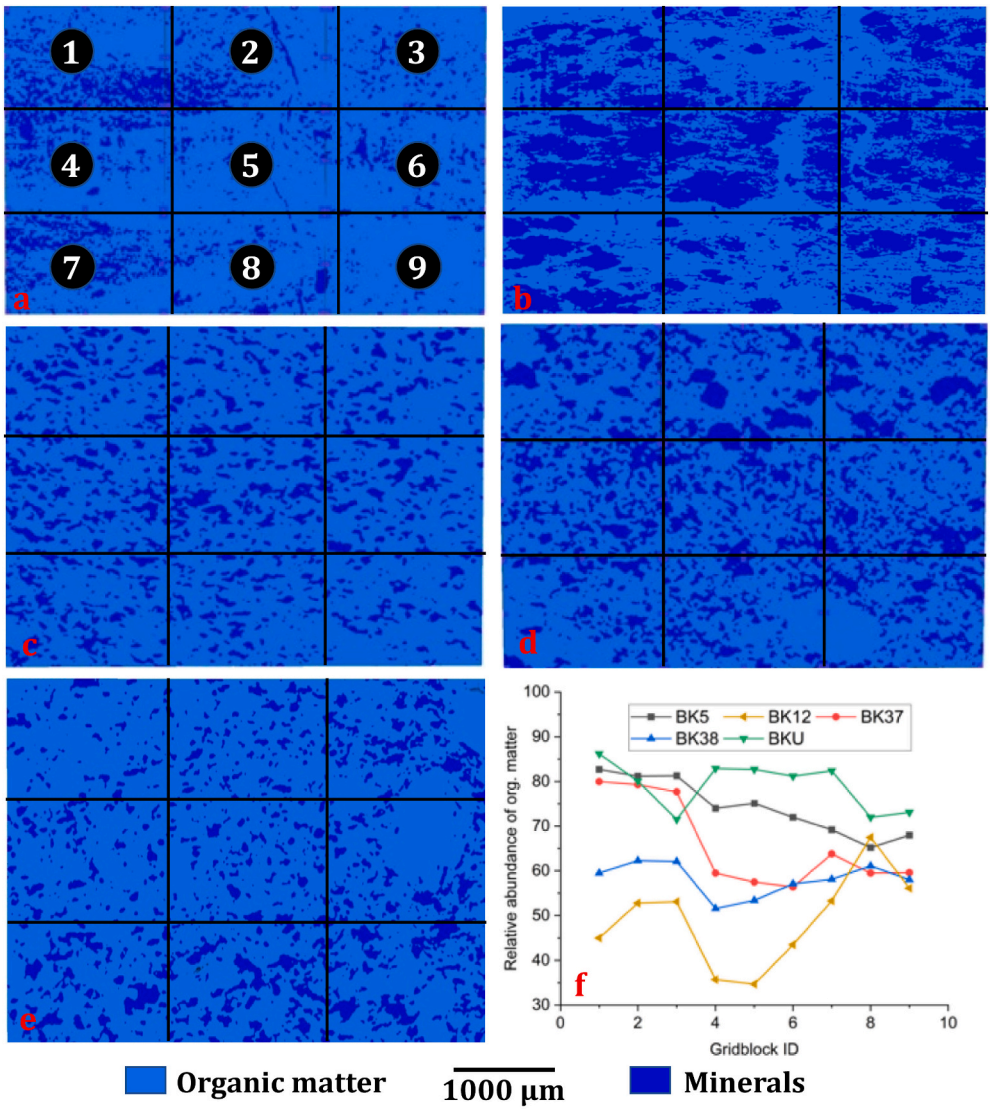

Fig. 5. Reconstructed and segmented X-ray CT image volume. (a-e) sequentially represent BK5, BK12, BK37, BK38 and BKU. The numbering scheme of grid units is shown in (a). (f) represents the relative abundance of organic matter (%) across different grid units.

in the unique axis concerning the unique axis of the first scan. The axis of orientation of the 2D SAXS profiles concerning the first scan for each shale sample the organic-rich shale sample (Table S1 and Fig. 7c and f) and varies at different scan points. The maximum angular deviation in the anisotropy axis for organic-rich shales BK5 and BK12 is ~5.5 and 19°, respectively. Similarly, spatial distribution in the axis of pore alignment for organic lean shale sample (Table S1, Fig. 8c, f, and i) and show significant variations. The maximum angular deviation in organic lean shales BK37, BK38, and BKU is ~17°, 14°, and 12°, respectively. Thus, angular deviation in the anisotropy axis does not correlate with the TOC and thermal maturity.

The spatial distribution in the degree of orientation for organic-rich shale (Fig. 7b, e) significantly varies in the range of 0.3 to 0.5 with a maximum change of ~60%. Spatial distribution in the orientation for organic lean shale (Fig. 8b, e, and h) indicate that variation in the degree of the anisotropy for BK37 is the least and in the range of 0.25 to 0.32 with a maximum change of 28%. The BK38 shale shows a very poor anisotropy which is evident from the flat azimuthal scattering profiles and the degree of the orientation varies in the range of 0.02 to 0.2. The spatial variation in the degree of the anisotropy is large and its value is close to zero at some point indicating no pore alignment at some other point, the value of the degree of anisotropy is ~0.2, which shows partial pore orientations in the bedding plane. The degree of the pore anisotropy in the BKU shale is higher than in BK37 but remains lower than in organic-rich shales BK5 and BK12. The spatial variation in the anisotropy of BKU shale is lower as evident from the contour map in Fig. 8 h and the degree of anisotropy varies in the range of 0.34 to 0.31 with a maximum variation of 9%.

Another approach to the estimation of the degree of anisotropy in the shale relies on the fitting of the azimuthal intensity profile with an analytical function. For a power law scattering with fixed exponent α, the Q dependence of the scattering is separable from the azimuthal dependence and the azimuthal scattering profile is (Gu and Mildner, 2016),

$$I(Q,\Phi) \cong C\left[\left(a^{-2}cos^2\Phi + b^{-2}sin^2\Phi\right)^{1/2}Q\right]^{-\alpha} \quad (2)$$

where a and b are the semi-major and semi-minor axes of the 2D elliptical SAXS pattern, respectively, and Φ is the azimuthal angle. C is a scaling constant. The eccentricity parameter, $\varepsilon = \sqrt{1-(a/b)^2}$. The Eq. (2) is valid only if the Q dependence does not change over the Q range considered for azimuthal integration. As shown in Fig. 5d, the exponent of the scattering profile remains constant in the Q-range of 0.4 to 1.3

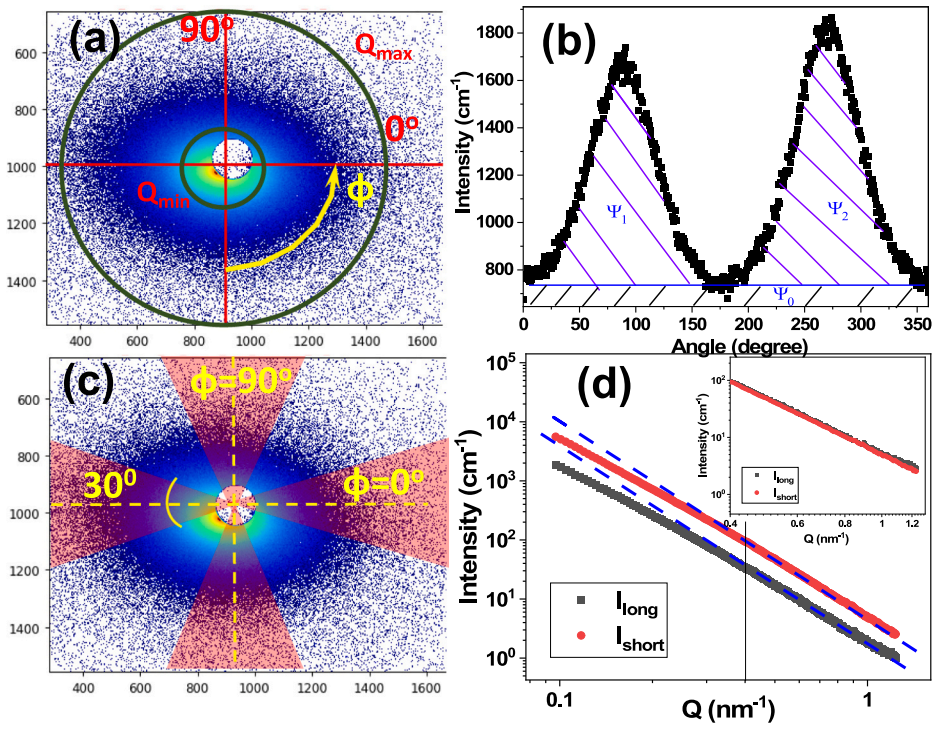

Fig. 6. (a) 2D SAXS profile of BK5 shale section cut perpendicular to the bedding plane. The annular region of azimuthal integration is shown with the inner and outer circles, that correspond to the $Q_{min} \sim 0.4$ nm^{-1} and $Q_{max} \sim 1.3$ nm^{-1}, respectively. (b) The scattering intensity I(Φ) is depicted as a function of the azimuthal angle Φ for the elliptical 2D SAXS patterns (c) 2D SAXS profiles with marked sectors of 30° for which radial integration is performed to get the scattering intensity along the long axis(Φ = 0°) and short axis (Φ = 90°) (d) Radially averaged scattering intensity along the long axis, I_{long} and short axis I_{short}. The slope of the SAXS profiles in the Q-range of 0.4 to 1.3 nm^{-1} is identical as also evident from the inset.

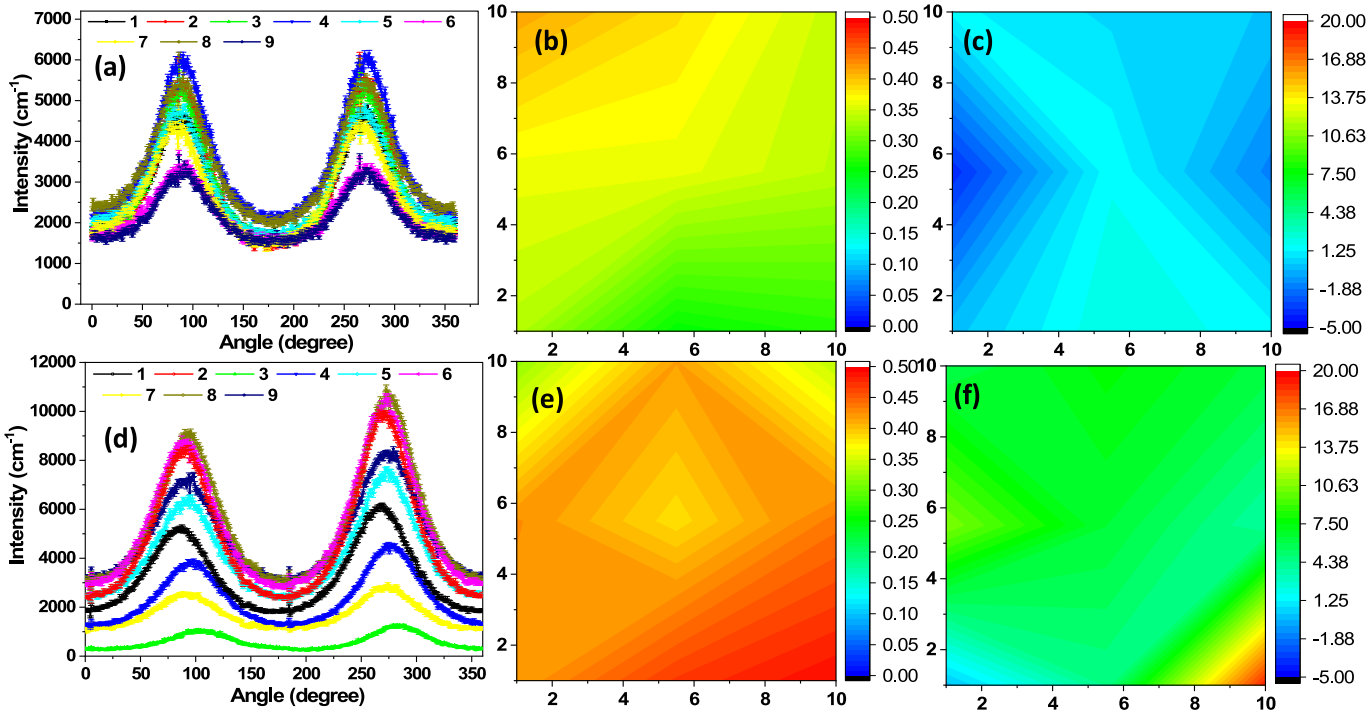

Fig. 7. (a, d) Azimuthal intensity profiles of BK5 and BK12 respectively. (b, e) Spatial distribution of the degree of orientation of BK5 and BK12 respectively in the scale of 0 to 0.5. (c, f) The orientation angle spatial distributions of BK5 and BK12 on the scale of − 5° to 20°.

nm^{-1}. Since the azimuthal averaging of 2D SAXS profiles has been carried out in this Q-range, therefore, Eq. (2) is valid for the analysis. The Eq. (2) is further simplified as shown below to fit the experimental azimuthal intensity profile,

$$I(\Phi) \cong C' \left[\left(cos^2\Phi + (a/b)^2 sin^2\Phi \right) \right]^{-\alpha/2} \quad (3)$$

The fitting of Eq. (3) to the experimental azimuthal scattering profile gives the value of the a/b. C' is the scaling constant. The fitting of the Eq. (3) to the azimuthal intensity profiles were carried out for each scan for all the shale samples. The fitting of the Eq. (3) to the azimuthal intensity profiles for BK5 shale have been depicted in Fig. S2. The a/b ratio is estimated and the eccentricity parameter is calculated.

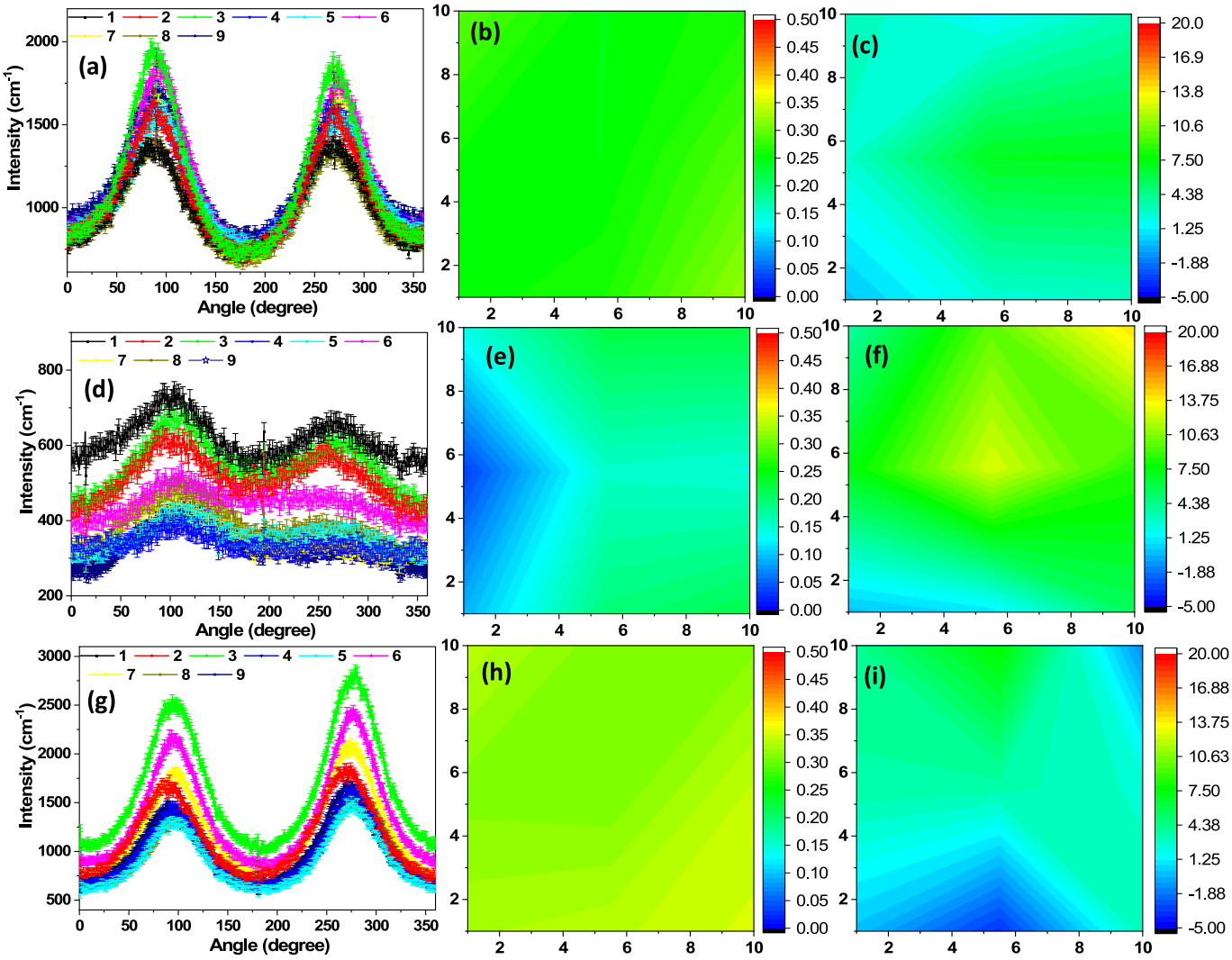

Fig. 8. (a, d, g) Azimuthal intensity profiles of BK37, BK38, and BKU respectively. (b, e, h) Spatial distribution of the degree of orientation of BK37, BK38, and BKU, respectively in the scale of 0 to 0.5 (c, f, i) Spatial distribution of the orientation angle of BK37, BK38, and BKU in the scale of − 5° to 20°.

4.1.2. Iso-size anisotropy

Iso-size anisotropy analysis (Blach et al., 2020; Gu and Mildner, 2016) is a method to study the anisotropy of the pore structure using 2D SAXS profiles. This method compares the scattering intensity, I(Q) as a function of the scattering vector, Q obtained by radial averaging of the 2D SAXS pattern in different sectors preferably along the major and minor axis. By analyzing the variations in intensity across different sectors, it is possible to identify a pore size-dependent anisotropy. This information can be used to extract the anisotropy parameter, which characterizes the pore orientation. Iso-size anisotropy analysis provides a more detailed characterization of the pore alignment in shale and is more effective than conventional methods, such as azimuthally averaged SAXS profiles, in extracting information about the pore structure from SAXS data (Blach et al., 2020). It is assumed that the scattering behavior of shale is a power law in nature, i.e. $I(Q) \sim Q^{-\alpha}$. Further, it is also assumed that α does not change in the probed Q-range. α is an exponent, which varies between 3 and 4 indicating that rock matrix and pore space are fractal (Radlinski, 2006; Wong et al., 1986). Surface fractal dimension is a mathematical concept that describes the roughness or irregularity of a surface. Specifically, it measures the degree to which the surface appears fragmented or self-similar at different scales. A fractal dimension is a non-integer number that can range between 2 (a smooth, flat surface with no irregularities) and 3 (a very rough, irregular surface with many bumps, pores, and other features at different scales). The value of the surface fractal dimension D_s is related to the power law exponent as $\alpha = 6\text{-}D_s$ (Wong et al., 1986).

The isosize anisotropy ratio is defined (Gu and Mildner, 2016) as $\zeta = I_{short}/I_{long}$. The I_{short} and I_{long} are the radially integrated scattering intensity corresponding to azimuthal angle $\Phi = 90^o$ and 0^o, respectively as depicted in Fig. 6c, d. The high-Q flat scattering is subtracted from SAXS data before analysis. Sectorial radially averaged scattering intensity of 2D SAXS profiles along the major axis and minor axis, respectively at different scan positions for organic-rich BK5 and BKU shale (Fig. 9a-d and b-e) is utilized to estimate isosize anisotropy parameter ζ as a function of Q and pore size (2.5/Q) (Fig. 9c, f). The isosize anisotropy parameter ζ shows large spatial variation for the BK5 sample and it varies between ~2–4 that follows a similar trend shown by the degree of anisotropy discussed earlier. Interestingly, the ζ parameter varies with Q indicating the extent of the anisotropy depends on the pore size. For the BK5 sample, it is observed from Fig. 9c that anisotropy first decreases with an increase in pore size and remains more or less constant over a large size range of the pores and subsequently, it decreases for pore size <10 nm.

The spatial variation in the isosize anisotropy parameter for low-matured organic-rich BK12 shale is less compared to thermally matured BK5 shale. The isosize anisotropy parameter is less than that for BK5 shale. Interestingly, the Q-dependence of ζ shows a different trend than BK5. ζ decreases with increasing pore size in the beginning and

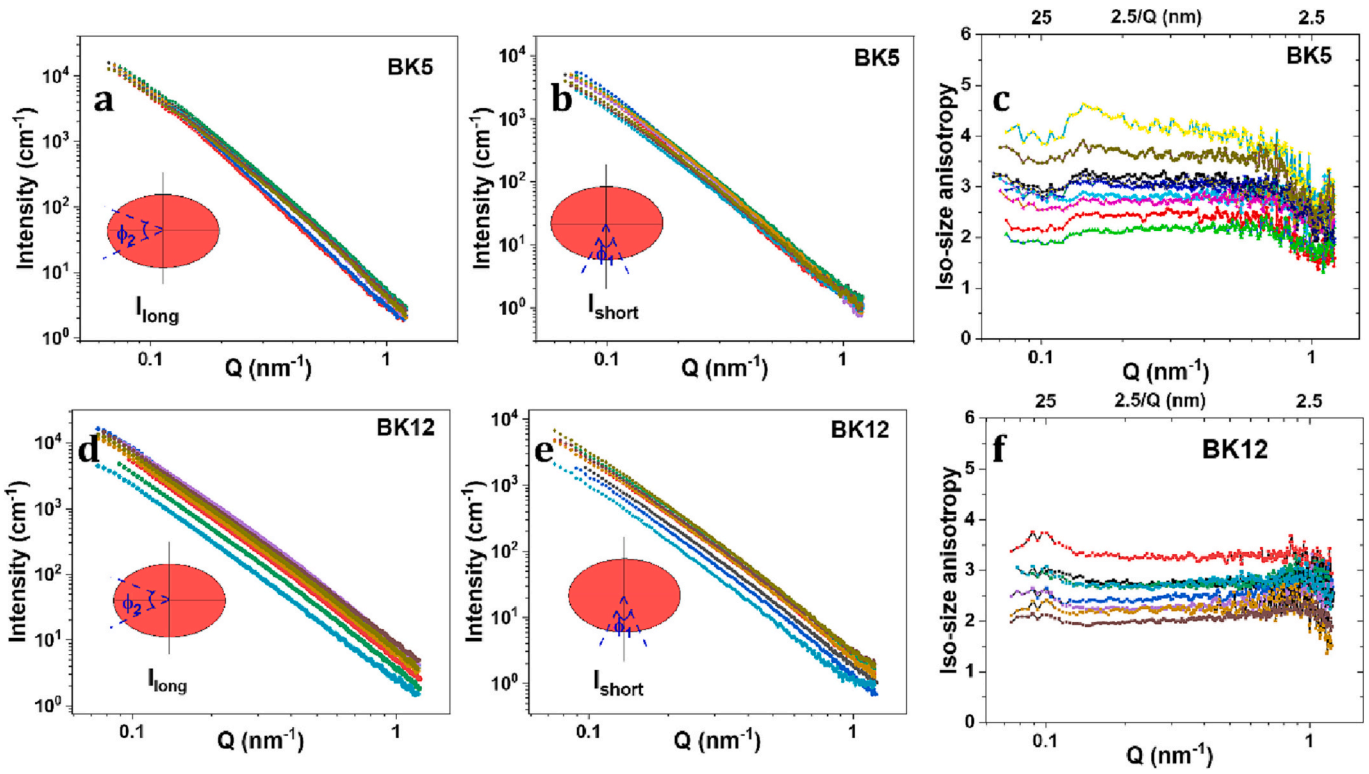

Fig. 9. Iso-size isotropy analysis of the organic-rich BK5 and BK12 shales and spatial heterogeneity in isosize anisotropy. (a, d) The scattering intensity I_{long} was obtained by sectorial radially averaging along the major axis of 2D SAXS profiles (inset) for different scan positions. (b, e) The scattering intensity I_{short} obtained by sectorial radially averaging along the minor axis of 2D SAXS profiles (inset) for different scan positions. (c, f) Q-variation of isosize anisotropy parameter ζ at different scan positions.

remains constant for most of the pore sizes except at large-Q where ζ decreases slightly.

The isosize anisotropy analysis for BK37, BK38, and BKU having relatively low organic matter is shown in Fig. 10. In general, the ζ value for three shales remains less compared to the organic-rich BK5 and BK12 shales. The value of ζ for BK38 is nearly one indicating the absence of pore anisotropy. Further, the spatial variation in isosize anisotropy of BK37, BK38, and BKU is found to be less compared to the organic-rich shales.

4.2. Correlation between organic matter content and pore anisotropy

Pore orientation in the shales depends on the organic matter content. The compositional anisotropy across the nine sections of the shale sample indicates BK5 and BK12 have the highest variation in organic matter distribution (Fig. 5f), also have the highest variation in isosize (Fig. 9c, f) and azimuthal (Fig. 7 a, d) anisotropy. The ATR-FTIR map of the shale surface indicates higher abundance and uneven distribution of organic matter in BK5 and BK12 (Fig. 3a, b).

A relation between X-ray transmission and TOC is observed in Fig. 11a. The transmission of X-rays increases with increasing TOC. The linear adsorption coefficient for X-rays for organic matter is less therefore transmission of X-rays increases for the shale with higher TOC. The anisotropy parameters (ρ, ε, ζ) obtained from various approaches show a correlation with TOC (Fig. 11 b-d). To establish the nature of correlation with TOC, a large number of shales with varying TOC with similar thermal maturity needs to be explored.

Pores in the organic-rich shales BK5 and BK12 show a higher degree of orientation and wide variation in the direction of pore orientation. The majority of *meso* and micropores in organic-rich shale are embedded in the organic matter of shale (King Jr et al., 2015; Mastalerz et al., 2012; Zhang et al., 2022). Due to the lower strength of organic matter concerning minerals, pores confined in organic matter are more amenable to deformation. The large variation in the degree of pore orientation within the shale sample is directly linked to the distribution of the organic matter in the BK5, and BK12 shales evident from the X-ray CT images and FTIR functional maps.

The organic content in BK37, BK38, and BKU is low and evenly distributed (Fig. 3c-e), which contributes to the homogeneity in pore attributes across bedding planes. Therefore, pore anisotropy is less due to the high compressive strength of the mineral matter compared to organic matter. Although the mineral and organic matter show preferential elongation parallel to bedding planes (Fig. 5c-e), the high compressive strength of the mineral matter resists pore deformation under compressive stress leading to less anisotropy in the organic-lean shales.

We also determined the distribution of organic matter from the X-ray CT images using the "Label analysis" module in Avizo (AVIZO, 2009). After obtaining the thresholded organic matter fraction in 3D, the application of the label analysis module separates each connected organic matter patch based on its connectivity. Two or more adjacent organic matter patches are detached by determining their local maxima in gray value at their interface based on Watershed segmentation (Levner and Zhang, 2007). Two or more neighboring organic matter patches within a 6-voxel distance are assumed as a single entity. The length of each organic matter patch along the vertical and horizontal direction was obtained from the post-processing of the resultant labeled image. The anisotropy of the organic matter patches was calculated as the ratio of the length of the patches along the horizontal axis (parallel to the bedding plane) to the length of the patches along the vertical axis (perpendicular to the bedding plane) (Fig. 12). For simplicity we can call this ratio as the degree of anisotropy, where a higher ratio indicates elongation of organic matter patches along the bedding plane, whereas a lower ratio indicates organic matter elongated across the bedding plane.

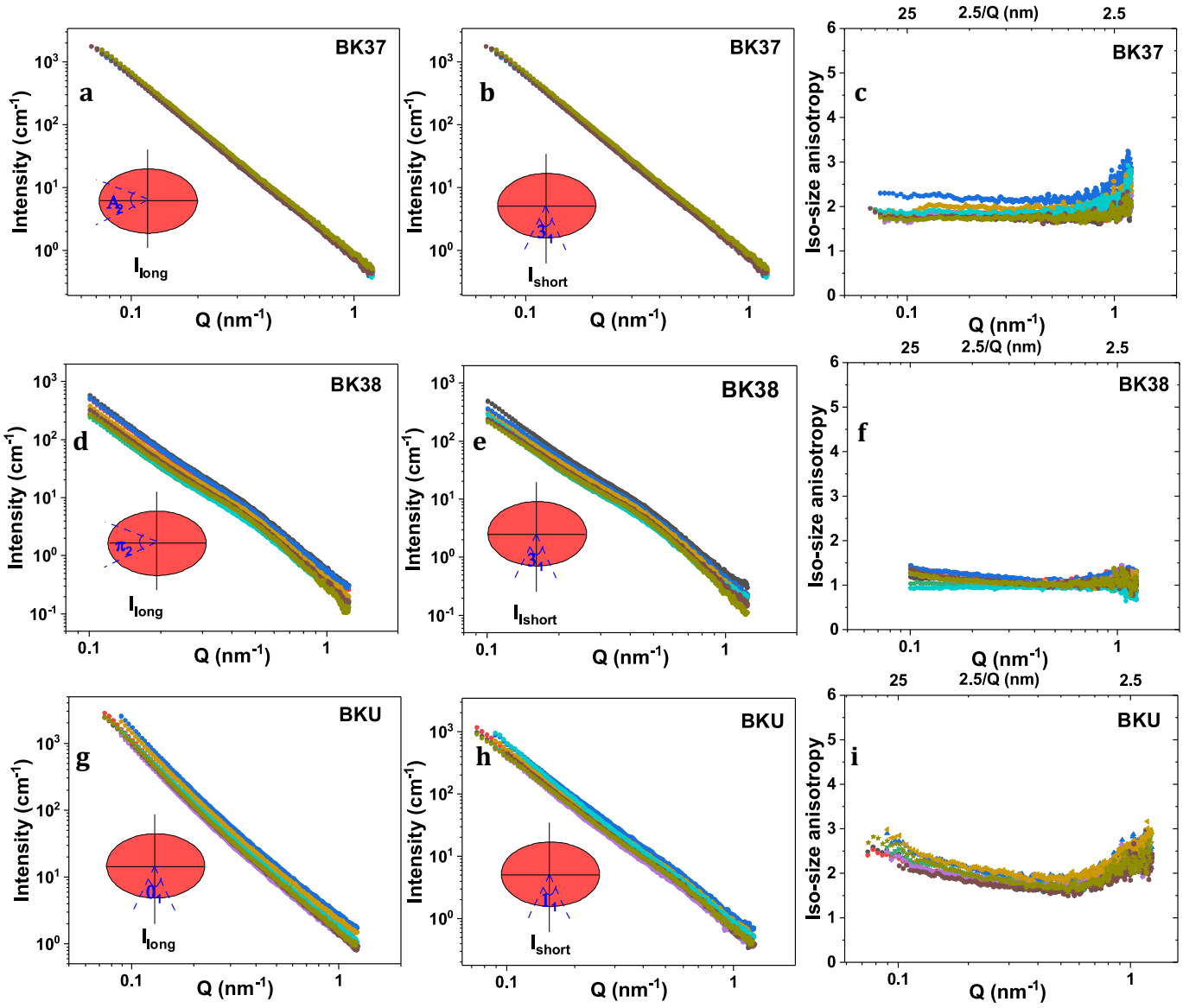

Fig. 10. Iso-size isotropy analysis of the organic-rich BK37, BK38, and BKU shales and spatial heterogeneity in isosize anisotropy. (a, d, g) The scattering intensity I_{long} was obtained by sectorial radially averaging along the major axis of 2D SAXS profiles (inset) for different scan positions. (b, e, h) The scattering intensity I_{short} obtained by sectorial radially averaging along the minor axis of 2D SAXS profiles (inset) for different scan positions. (c, f, i) Q-variation of isosize anisotropy parameter ζ at different scan positions.

A ratio close to 1 indicates no preferential orientation for the organic matter. A typical higher degree of anisotropy is observed in the high TOC shales (BK5 and BK12), whereas a typical normal distribution is observed for the low TOC shales (BK37, BK38, and BKU), which validates our SAXS observations.

5. Conclusions

Detailed studies on the orientation of minerals, organic matter, and nanopores in shales across bedding planes using SAXS, X-ray μCT, and ATR-FTIR functional group mapping show a relation with organic matter content. The X-ray μCT and FTIR provide information on the heterogeneity and orientation of minerals/organic matter in the micrometer length scale. The transmission of the X-ray in SAXS measurements and X-ray radiographs provided information on micrometer size heterogeneity in the shale. Two methodologies have been adopted for the analysis of 2D anisotropic SAXS patterns to examine pore orientation in shale.

The degree of pore orientation in shale samples with higher organic content is higher than that for the shale samples with lower organic content. The high degree of pore orientation in organic-rich shales is attributed to a higher deformability of the rock resulting in a reshaping of the pore structure under compaction. Similar signatures are also evident from FTIR mapping and X-ray CT imaging, where preferential elongation of organic matter parallel to the bedding plane was observed. The distribution of organic matter is also highly heterogeneous in shales having high TOC. The abundance of organic matter across the bedding plane differs by ~11% and ~ 15% for organic-rich shales, as compared to ~5% for organic-lean shales. The isosize analysis also shows that organic-rich shales possess higher pore alignment compared to organic-lean shales with significant variations within each shale sample. This study suggests that the vertical anisotropy in shale fabric plays an important role in the localization of pores, and how the bulk organic properties (TOC, Tmax) are linked to it. The anisotropy in pore orientation originates from overburden pressure and correlates with TOC.

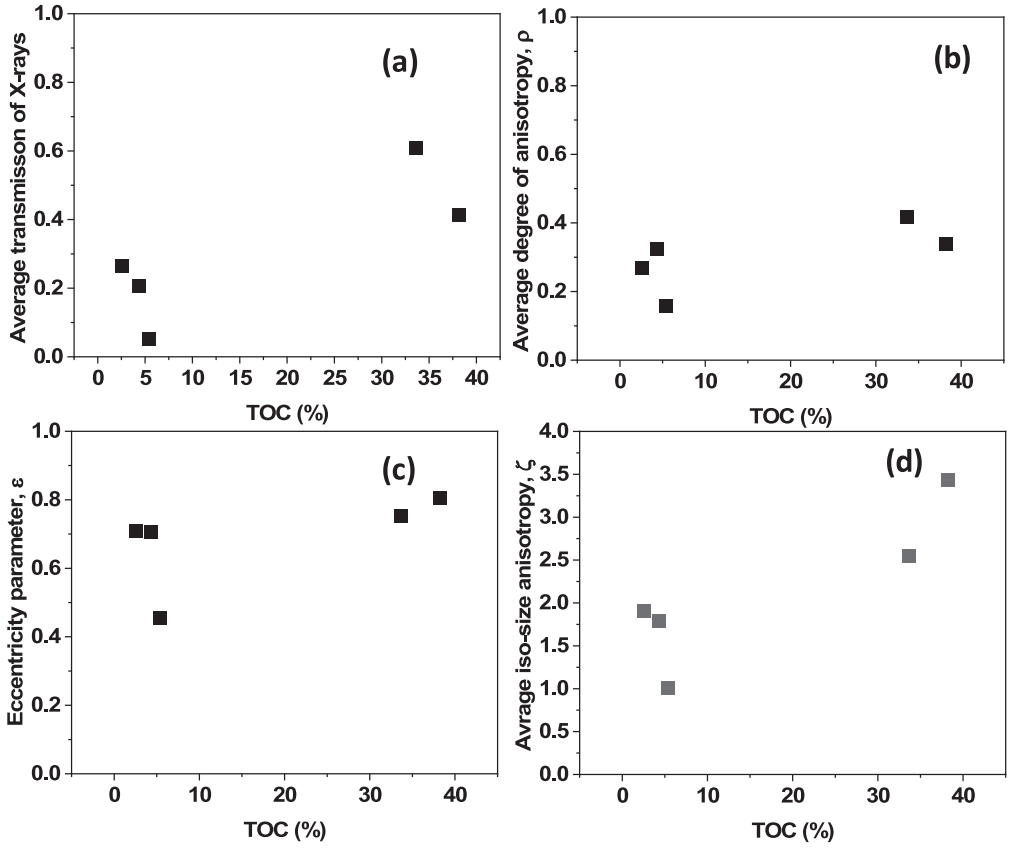

Fig. 11. Correlation of (a) X-ray transmission (b) degree of anisotropy, ρ (c) eccentricity parameters, and (a) isosize anisotropy parameter, ζ with TOC of the shale.

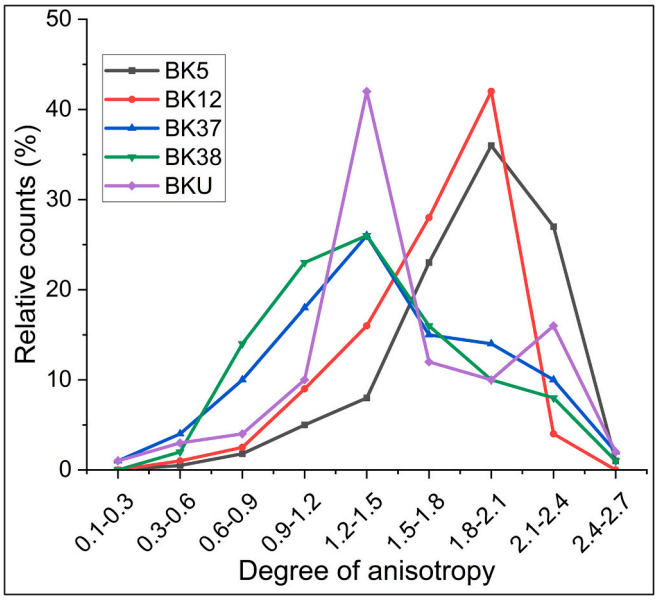

Fig. 12. Degree of anisotropy of organic matter patches weighted by their frequency as determined from X-ray CT images.

CRediT authorship contribution statement

Jitendra Bahadur: Conceptualization, Methodology, Formal analysis, Investigation, Writing – original draft, Supervision. **Debanjan Chandra:** Methodology, Validation, Investigation, Writing – original draft. **Avik Das:** Software, Formal analysis, Investigation, Visualization. **Vikram Vishal:** Conceptualization, Resources, Writing – review & editing. **Ashish Kumar Agrawal:** Investigation. **Debasis Sen:** Writing – review & editing.

Declaration of Competing Interest

The authors declare that they have no known competing financial interests or personal relationships that could have appeared to influence the work reported in this paper.

Data availability

Data will be made available on request.

Acknowledgments

VV acknowledges the funds support received under BRNS Young Achiever Award Grant (Project Code Number: 58/20/23/2019-BRNS; RD/0119-BRNS000-002). The authors would also like to acknowledge Sophisticated Analytical Instrumentation Facility (SAIF), IIT Bombay for facilitating ATR-FTIR imaging. Authors thank Dr. S.M. Yusuf, Head, Solid State Physics Division and Director, Physics Group, BARC and Dr. V.K. Aswal, Head, Mesoscopic Small Angle Scattering section, Solid State Physics Division, BARC for their encouragement and support towards SWAXS beamline, Indus-2.

Appendix A. Supplementary data

Supplementary data to this article can be found online at https://doi.org/10.1016/j.coal.2023.104268.

References

Agrawal, A., Singh, B., Kashyap, Y., Shukla, M., Sarkar, P., Sinha, A.N., 2015. Design, development and first experiments on the X-ray imaging beamline at Indus-2 synchrotron source RRCAT, India. J. Synchrotron Radiat. 22, 1531–1539.

Al Shafloot, T., Kim, T.W., Kovscek, A.R., 2021. Investigating fracture propagation characteristics in shale using sc-CO2 and water with the aid of X-ray Computed Tomography. J. Na. Gas Sci. Eng. 92, 103736.

Anovitz, L.M., Cole, D.R., Sheets, J.M., Swift, A., Elston, H.W., Welch, S., Chipera, S.J., Littrell, K.C., Mildner, D.F.R., Wasbrough, M.J., 2015. Effects of maturation on multiscale (nanometer to millimeter) porosity in the Eagle Ford Shale. Interpretation 3, SU59-SU70.

Arif, M., Mahmoud, M., Zhang, Y., Iglauer, S., 2021. X-ray tomography imaging of shale microstructures: a review in the context of multiscale correlative imaging. Int. J. Coal Geol. 233, 103641.

Avizo, V., 2009. Visilog 6, Reference Guide.

Bahadur, J., Melnichenko, Y., Mastalerz, M., Furmann, A., Clarkson, C.R., 2014. Hierarchical pore morphology of cretaceous shale: a small-angle neutron scattering and ultrasmall-angle neutron scattering study. Energy Fuel 28, 6336–6344.

Bahadur, J., Radlinski, A.P., Melnichenko, Y.B., Mastalerz, M., Schimmelmann, A., 2015. Small-angle and ultrasmall-angle neutron scattering (SANS/USANS) study of New Albany Shale: a treatise on microporosity. Energy Fuel 29, 567–576.

Bahadur, J., Medina, C.R., He, L., Melnichenko, Y.B., Rupp, J.A., Blach, T.P., Mildner, D. F., 2016. Determination of closed porosity in rocks by small-angle neutron scattering. J. Appl. Crystallogr. 49, 2021–2030.

Bahadur, J., Ruppert, L.F., Pipich, V., Sakurovs, R., Melnichenko, Y.B., 2018. Porosity of the Marcellus Shale: a contrast matching small-angle neutron scattering study. Int. J. Coal Geol. 188, 156–164.

Bahadur, J., Das, A., Sen, D., 2019. Evaporation-induced structural evolution of the lamellar mesophase: a time-resolved small-angle X-ray scattering study. J. Appl. Crystallogr. 52, 1169–1175.

Bhandari, A.R., Flemings, P.B., Polito, P.J., Cronin, M.B., Bryant, S.L., 2015. Anisotropy and stress dependence of permeability in the Barnett shale. Transp. Porous Media 108, 393–411.

Bhattacharjee, J., Ghosh, K.K., Bhattacharya, B., 2018. Petrography and geochemistry of sandstone–mudstone from Barakar Formation (early Permian), Raniganj Basin, India: Implications for provenance, weathering and marine depositional conditions during lower Gondwana sedimentation. Geol. J. 53, 1102–1122.

Bhattacharya, B., Bandyopadhyay, S., Mahapatra, S., Banerjee, S., 2012. Record of tide-wave influence on the coal-bearing Permian Barakar Formation, Raniganj Basin, India. Sediment. Geol. 267, 25–35.

Blach, T., Radlinski, A.P., Edwards, D.S., Boreham, C.J., Gilbert, E.P., 2020. Pore anisotropy in unconventional hydrocarbon source rocks: a small-angle neutron scattering (SANS) study on the Arthur Creek Formation, Georgina Basin, Australia. Int. J. Coal Geol. 225, 103495.

Busch, A., Alles, S., Gensterblum, Y., Prinz, D., Dewhurst, D.N., Raven, M.D., Stanjek, H., Krooss, B.M., 2008. Carbon dioxide storage potential of shales. Int. J. Greenhouse Gas Control 2, 297–308.

Cao, G., Lin, M., Ji, L., Jiang, W., Yang, M., 2019. Characterization of pore structures and gas transport characteristics of Longmaxi shale. Fuel 258, 116146.

Chalmers, G.R., Bustin, R.M., 2007. The organic matter distribution and methane capacity of the lower cretaceous strata of Northeastern British Columbia, Canada. Int. J. Coal Geol. 70, 223–239.

Chalmers, G.R., Bustin, R.M., Power, I.M., 2012. Characterization of gas shale pore systems by porosimetry, pycnometry, surface area, and field emission scanning electron microscopy/transmission electron microscopy image analyses: examples from the Barnett, Woodford, Haynesville, Marcellus, and Doig units. AAPG Bull. 96, 1099–1119.

Chandra, D., Vishal, V., 2020. A comparison of nano-scale pore attributes of Barakar Formation gas shales from Raniganj and Wardha Basin, India using low pressure sorption and FEG-SEM analysis. J. Nat. Gas Sci. Eng. 81, 103453.

Chandra, D., Vishal, V., 2021. A critical review on pore to continuum scale imaging techniques for enhanced shale gas recovery. Earth Sci. Rev. 217, 103638.

Chandra, D., Vishal, V., Bahadur, J., Sen, D., 2020a. A novel approach to identify accessible and inaccessible pores in gas shales using combined low-pressure sorption and SAXS/SANS analysis. Int. J. Coal Geol. 228, 103556.

Chandra, D., Vishal, V., Debbarma, A., Banerjee, S., Pradhan, S.P., Mishra, M.K., 2020b. Role of composition and depth on pore attributes of Barakar Formation Gas Shales of Ib Valley, India, using a combination of low-pressure sorption and image analysis. Energy Fuel 34, 8085–8098.

Chandra, D., Vishal, V., Bahadur, J., Agrawal, A.K., Das, A., Hazra, B., Sen, D., 2022. Nano-scale physicochemical attributes and their impact on pore heterogeneity in shale. Fuel 314, 123070.

Chandra, D., Bakshi, T., Bahadur, J., Hazra, B., Vishal, V., Kumar, S., Sen, D., Singh, T., 2023. Pore morphology in thermally-treated shales and its implication on CO2 storage applications: a gas sorption, SEM, and small-angle scattering study. Fuel 331, 125877.

Chareonsuppanimit, P., Mohammad, S.A., Robinson Jr., R.L., Gasem, K.A., 2012. High-pressure adsorption of gases on shales: Measurements and modeling. Int. J. Coal Geol. 95, 34–46.

Chen, B., Han, X., Jiang, X., 2016. In situ FTIR analysis of the evolution of functional groups of oil shale during pyrolysis. Energy Fuel 30, 5611–5616.

Cui, J., Si, G., 2021. Equivalent anisotropic permeability of shale rocks: effect of micro-fractures. J. Pet. Sci. Eng. 207, 109085.

Duan, Y., Feng, X.-T., Li, X., Yang, B., 2022. Mesoscopic damage mechanism and a constitutive model of shale using in-situ X-ray CT device. Eng. Fract. Mech. 269, 108576.

Fan, C., Yan, J., Huang, Y., Han, X., Jiang, X., 2015. XRD and TG-FTIR study of the effect of mineral matrix on the pyrolysis and combustion of organic matter in shale char. Fuel 139, 502–510.

Fratzl, P., Groschner, M., Vogl, G., Plenk Jr., H., Eschberger, J., Fratzl-Zelman, N., Koller, K., Klaushofer, K., 1992. Mineral crystals in calcified tissues: a comparative study by SAXS. J. Bone Miner. Res. 7, 329–334.

Gasparik, M., Ghanizadeh, A., Bertier, P., Gensterblum, Y., Bouw, S., Krooss, B.M., 2012. High-pressure methane sorption isotherms of black shales from the Netherlands. Energy Fuel 26, 4995–5004.

Gasparik, M., Bertier, P., Gensterblum, Y., Ghanizadeh, A., Krooss, B.M., Littke, R., 2014. Geological controls on the methane storage capacity in organic-rich shales. Int. J. Coal Geol. 123, 34–51.

Gu, X., Mildner, D., 2016. Ultra-small-angle neutron scattering with azimuthal asymmetry. J. Appl. Crystallogr. 49, 934–943.

Gu, X., Cole, D.R., Rother, G., Mildner, D.F., Brantley, S.L., 2015. Pores in Marcellus shale: a neutron scattering and FIB-SEM study. Energy Fuel 29, 1295–1308.

Hall, P.L., Mildner, D., 1983. On the analysis of small-angle scattering with elliptical azimuthal symmetry. J. Appl. Phys. 54, 427–428.

Hazra, B., Singh, D.P., Chakraborty, P., Singh, P.K., Sahu, S.G., Adak, A.K., 2021. Using rock-eval S4Tpeak as thermal maturity proxy for shales. Mar. Pet. Geol. 127, 104977.

He, L., Melnichenko, Y.B., Mastalerz, M., Sakurovs, R., Radlinski, A.P., Blach, T., 2012. Pore accessibility by methane and carbon dioxide in coal as determined by neutron scattering. Energy Fuel 26, 1975–1983.

He, R., Ren, L., Zhang, R., Zhu, Z., Sun, X., 2022. Anisotropy characterization of the elasticity and energy flow of Longmaxi shale under uniaxial compression. Energy Rep. 8, 1410–1424.

Ji, W., Song, Y., Rui, Z., Meng, M., Huang, H., 2017. Pore characterization of isolated organic matter from high matured gas shale reservoir. Int. J. Coal Geol. 174, 31–40.

Kang, S.M., Fathi, E., Ambrose, R.J., Akkutlu, I.Y., Sigal, R.F., 2011. Carbon dioxide storage capacity of organic-rich shales. SPE J. 16, 842–855.

King Jr., H.E., Eberle, A.P., Walters, C.C., Kliewer, C.E., Ertas, D., Huynh, C., 2015. Pore architecture and connectivity in gas shale. Energy Fuel 29, 1375–1390.

Kwiecińska, B., Pusz, S., Valentine, B.J., 2019. Application of electron microscopy TEM and SEM for analysis of coals, organic-rich shales and carbonaceous matter. Int. J. Coal Geol. 211, 103203.

Kwon, O., Kronenberg, A.K., Gangi, A.F., Johnson, B., Herbert, B.E., 2004. Permeability of illite-bearing shale: 1. Anisotropy and effects of clay content and loading. J. Geophys. Res. Solid Earth 109.

Lafargue, E., Marquis, F., Pillot, D., 1998. Rock-Eval 6 applications in hydrocarbon exploration, production, and soil contamination studies. Rev. l'instit. Français pétrole 53, 421–437.

Leu, L., Georgiadis, A., Blunt, M.J., Busch, A., Bertier, P., Schweinar, K., Liebi, M., Menzel, A., Ott, H., 2016. Multiscale description of shale pore systems by scanning SAXS and WAXS microscopy. Energy Fuel 30, 10282–10297.

Levner, I., Zhang, H., 2007. Classification-driven watershed segmentation. IEEE Trans. Image Process. 16, 1437–1445.

Lewis, E.N., Treado, P.J., Reeder, R.C., Story, G.M., Dowrey, A.E., Marcott, C., Levin, I. W., 1995. Fourier transform spectroscopic imaging using an infrared focal-plane array detector. Anal. Chem. 67, 3377–3381.

Liu, H.-H., 2014. Non-Darcian flow in low-permeability media: key issues related to geological disposal of high-level nuclear waste in shale formations. Hydrogeol. J. 22, 1525–1534.

Ma, Y., Pan, Z., Zhong, N., Connell, L.D., Down, D.I., Lin, W., Zhang, Y.L., 2016. Experimental study of anisotropic gas permeability and its relationship with fracture structure of Longmaxi Shales, Sichuan Basin, China. Fuel 180, 106–115.

Mastalerz, M., He, L., Melnichenko, Y.B., Rupp, J.A., 2012. Porosity of coal and shale: Insights from gas adsorption and SANS/USANS techniques. Energy Fuel 26, 5109–5120.

Neuzil, C., 2013. Can shale safely host US nuclear waste? EOS Trans. Am. Geophys. Union 94, 261–262.

Nie, H., Jin, Z., Zhang, J., 2018. Characteristics of three organic matter pore types in the Wufeng-Longmaxi Shale of the Sichuan Basin, Southwest China. Sci. Rep. 8, 1–11.

Radlinski, A.P., 2006. Small-angle neutron scattering and the microstructure of rocks. Rev. Mineral. Geochem. 63, 363–397.

Radlinski, A., Mastalerz, M., Hinde, A., Hainbuchner, M., Rauch, H., Baron, M., Lin, J., Fan, L., Thiyagarajan, P., 2004. Application of SAXS and SANS in evaluation of porosity, pore size distribution and surface area of coal. Int. J. Coal Geol. 59, 245–271.

Reynolds, L., Mildner, D., 1984. The elliptical average of small-angle scattering data. J. Appl. Crystallogr. 17, 411–416.

Rinnerthaler, S., Roschger, P., Jakob, H., Nader, A., Klaushofer, K., Fratzl, P., 1999. Scanning small angle X-ray scattering analysis of human bone sections. Calcif. Tissue Int. 64, 422–429.

Rouquerol, J., Avnir, D., Fairbridge, C.W., Everett, D.H., Haynes, J., Pernicone, N., Ramsay, J.D., Sing, K.S.W., Unger, K.K., 1994. Recommendations for the characterization of porous solids (Technical Report). Pure Appl. Chem. 66, 1739–1758.

Ruppert, L.F., Sakurovs, R., Blach, T.P., He, L., Melnichenko, Y.B., Mildner, D.F., Alcantar-Lopez, L., 2013. A USANS/SANS study of the accessibility of pores in the Barnett Shale to methane and water. Energy Fuel 27, 772–779.

Sayers, C.M., 2013. The effect of anisotropy on the Young's moduli and Poisson's ratios of shales. Geophys. Prospect. 61, 416–426.

Sen, S., Dey, J., 2019. A field-scale overview of facies architectures and depositional environment integrating core and geophysical log data: study from a marginal Gondwana Basin, India. J. Geol. Soc. India 94, 238–244.
Summerfield, G., Mildner, D., 1983. Small-angle scattering with azimuthal asymmetry. J. Appl. Crystallogr. 16, 384–389.
Turunen, M.J., Lages, S., Labrador, A., Olsson, U., Tägil, M., Jurvelin, J.S., Isaksson, H., 2014. Evaluation of composition and mineral structure of callus tissue in rat femoral fracture. J. Biomed. Opt. 19, 025003.
Varma, A.K., Mishra, D.K., Samad, S.K., Prasad, A.K., Panigrahi, D.C., Mendhe, V.A., Singh, B.D., 2018. Geochemical and organo-petrographic characterization for hydrocarbon generation from Barakar Formation in Auranga Basin, India. Int. J. Coal Geol. 186, 97–114.
Vishal, V., Chandra, D., 2022. Mechanical response and strain localization in coal under uniaxial loading, using digital volume correlation on X-ray tomography images. Int. J. Rock Mech. Min. Sci. 154, 105103.
Vishal, V., Chandra, D., Bahadur, J., Sen, D., Hazra, B., Mahanta, B., Mani, D., 2019. Interpreting pore dimensions in gas shales using a combination of SEM imaging, small-angle neutron scattering, and low-pressure gas adsorption. Energy Fuel 33, 4835–4848.
Wang, Y., Zhu, Y., Chen, S., Li, W., 2014. Characteristics of the nanoscale pore structure in Northwestern Hunan shale gas reservoirs using field emission scanning electron microscopy, high-pressure mercury intrusion, and gas adsorption. Energy Fuel 28, 945–955.
Wong, P.-Z., Howard, J., Lin, J.-S., 1986. Surface roughening and the fractal nature of rocks. Phys. Rev. Lett. 57, 637.
Yan, J., Jiang, X., Han, X., Liu, J., 2013. A TG–FTIR investigation to the catalytic effect of mineral matrix in oil shale on the pyrolysis and combustion of kerogen. Fuel 104, 307–317.
Yin, Y., Qu, Z., Zhang, T., Zhang, J., Wang, Q., 2020. Three-dimensional pore-scale study of methane gas mass diffusion in shale with spatially heterogeneous and anisotropic features. Fuel 273, 117750.
Zhang, X., Wang, J., Gao, F., Ju, Y., Engineering, 2017. Impact of water, nitrogen and CO2 fracturing fluids on fracturing initiation pressure and flow pattern in anisotropic shale reservoirs. J. Nat. Gas Sci. 45, 291–306.
Zhang, R., Liu, S., He, L., Blach, T.P., Wang, Y., 2020. Characterizing anisotropic pore structure and its impact on gas storage and transport in coalbed methane and shale gas reservoirs. Energy Fuel 34, 3161–3172.
Zhang, D., Zhang, X., Guo, H., Lin, D., Meegoda, J.N., Hu, L., 2021. An anisotropic pore-network model to estimate the shale gas permeability. Sci. Rep. 11, 7902.
Zhang, C., Yao, Y., Dong, Y., Engineering, 2022. Heterogeneous development of micro- and meso-pores in shale kerogen: New insights from chemical structure analysis. J. Nat. Gas Sci. 102, 104552.
Zhao, C., Hu, Q., Wang, Q., Ilavsky, J., Wang, M., Zhang, X., Yan, J., 2022. Multiple experimental studies of pore structure and mineral grain sizes of the Woodford shale in southern Oklahoma, USA. Front. Earth Sci. 10, 1787.